Multislip-enabled morphing of all-inorganic perovskites

Xiaocui Li [1,2,3,6], You Meng[2,6], Wanpeng Li [2,3,6], Jun Zhang [1], Chaoqun Dang [4], Heyi Wang [1], Shih-Wei Hung [2,3], Rong Fan [1], Fu-Rong Chen [2,3] ✉, Shijun Zhao [1] ✉, Johnny C. Ho [2] ✉ & Yang Lu [1,5] ✉

All-inorganic lead halide perovskites (CsPbX$_3$, X = Cl, Br or I) are becoming increasingly important for energy conversion and optoelectronics because of their outstanding performance and enhanced environmental stability. Morphing perovskites into specific shapes and geometries without damaging their intrinsic functional properties is attractive for designing devices and manufacturing. However, inorganic semiconductors are often intrinsically brittle at room temperature, except for some recently reported layered or van der Waals semiconductors. Here, by in situ compression, we demonstrate that single-crystal CsPbX$_3$ micropillars can be substantially morphed into distinct shapes (cubic, L and Z shapes, rectangular arches and so on) without localized cleavage or cracks. Such exceptional plasticity is enabled by successive slips of partial dislocations on multiple $\{110\}\langle 1\bar{1}0 \rangle$ systems, as evidenced by atomic-resolution transmission electron microscopy and first-principles and atomistic simulations. The optoelectronic performance and bandgap of the devices were unchanged. Thus, our results suggest that CsPbX$_3$ perovskites, as potential deformable inorganic semiconductors, may have profound implications for the manufacture of advanced optoelectronics and energy systems.

Semiconductor materials with substantial room-temperature plastic deformability can adapt to desirable shapes without losing targeted electronic performance, making them promising for developing deformable electronics. Their shapeability and mechanically adaptability lead to excellent processability and high conformability with other interfaces during device fabrication and helps to avoid brittle failure in practical use. The intrinsic softness and high deformability of organic semiconductors have led to applications in stretchable and deformable electronics[1]. However, the necessary molecular characteristics (such as high crystallinity) for desired charge transport could cause embrittlement[2]. On the other hand, inorganic semiconductors usually have higher carrier mobility and much better electrical performance

than organic semiconductors[3], but they are often brittle under ambient conditions due to their directional covalent bonds or the strong electrostatic interactions among ionic species[4]. When reduced to the micro- or nanoscale, in addition to substantially enhanced elasticity[5–8], a certain amount of intrinsic plasticity can be achieved at room temperature[9–12]. Nonetheless, substantial plastic deforming and shaping remain unattainable for most bulk inorganic semiconductors, except for a few single-crystal oxides with a high concentration of oxygen vacancies and pre-existing dislocations[13–17] and ZnS single crystals deformed in darkness[18], as well as recently reported bulk-layered and van der Waals semiconductors with extraordinary, metal-like, room-temperature plasticity[19–21] thanks to their weak interlayer bonding and easy gliding.

[1]Department of Mechanical Engineering, City University of Hong Kong, Kowloon, China. [2]Department of Materials Science and Engineering, City University of Hong Kong, Kowloon, China. [3]Time-resolved Aberration Corrected Environmental Electron Microscope Unit, City University of Hong Kong, Kowloon, China. [4]Center for X-mechanics, ZJU-Hangzhou Global Scientific and Technological Innovation Center, Zhejiang University, Hangzhou, China. [5]Department of Mechanical Engineering, The University of Hong Kong, Hong Kong, China. [6]These authors contributed equally: Xiaocui Li, You Meng, Wanpeng Li. ✉e-mail: frchen@cityu.edu.hk; shijzhao@cityu.edu.hk; johnnyho@cityu.edu.hk; ylu1@hku.hk
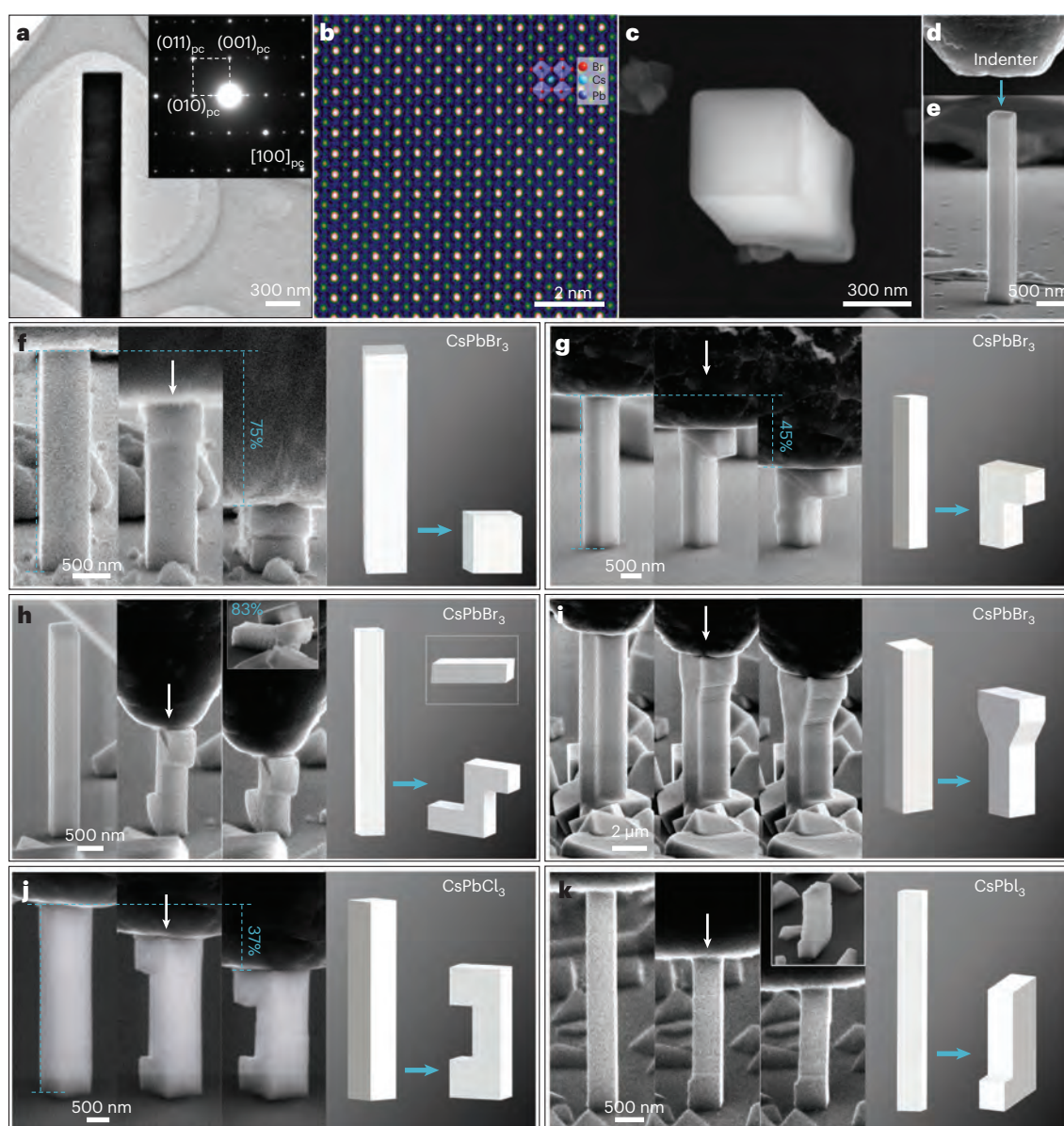
Fig. 1 | Material characterization, in situ experiment and morphing of CsPbX$_3$ single crystals into various geometries. a, Bright-field TEM image of a CsPbBr$_3$ single-crystal pillar. The inset is the selected-area electron diffraction pattern. **b**, Average background subtraction filtered HAADF-STEM image of CsPbBr$_3$. Elements are indicated by the superimposed unit cell. **c**, Top view of a CsPbBr$_3$ single-crystal pillar showing the square cross section. **d**,**e** SEM images of a flat punch diamond indenter (**d**) and a CsPbBr$_3$ pillar (**e**) grown vertically on the substrate, to illustrate the compression morphing process. **f**–**k**, Snapshots of in situ morphing of various CsPbBr$_3$ single crystals with different sizes into distinct shapes: cubic (**f**); upside-down L shape (**g**); Z shape (**h**); and wine glass (**i**). **j**, CsPbCl$_3$ single crystal. **k**, CsPbI$_3$ single crystal. Schematic diagrams of their original and deformed geometries are shown alongside the SEM snapshots.

Other than that, the plastic forming and morphing of inorganic semi-conductors into various shapes and geometries are still extremely attractive but uncommon. Realizing inorganic semiconductors with large room-temperature ductility remains a holy grail for fabricating complicated devices and deformable electronics.

Here, we report that single-crystal pillars of all-inorganic CsPbX$_3$ perovskites[22] grown by the vapour–liquid–solid method can have unusual intrinsic plastic deformability under ambient conditions. Unprecedented geometry and shape morphing can, thus, be achieved in situ through continuous mechanical compression, without affecting their optoelectronic performance or electronic band structures. Using atomic-resolution transmission electron microscopy (TEM) as well as first-principles and atomistic simulations, the successively and con-tinuously activated partial dislocations of multiple low-energy-barrier {110}⟨1$\bar{1}$0⟩ slip systems (multislipping) were verified as enabling the observed substantial plasticity. The strong Pb–X bonds maintain the crystal structural integrity and prevent cracking or cleaving. Such unprecedented plasticity and morphing can be consistently achieved in single-crystal pillar samples with various dimensions (diameter and length up to ~2 μm and 10 μm, respectively) and aspect ratios (~1.7–14). The corresponding compression strains, which are easily accommo-dated by multislipping, can be well above ~60–70%. The present results, together with the above-mentioned outstanding optoelectronic and energy conversion performance[23,24], indicate that CsPbX$_3$ perovskites are promising ductile semiconductors for advanced deformable elec-tronics and optoelectronics.

We first synthesized single-crystal CsPbX$_3$ pillars with diameters and widths of ~0.4 to 2 μm and lengths of ~3 to 10 μm via the vapour–liquid–solid method[25]. Figure 1a is a bright-field TEM image of a typical CsPbBr$_3$ pillar. The selected-area electron diffraction pattern in

the inset demonstrates the single crystallinity with an orthorhombic crystal structure[22]. By convention, the 'pseudocubic' CsPbX$_3$ perovskites are indexed by cubic structure (Supplementary Fig. 1) to simplify the deformation analysis[26]. Figure 1b shows an atomic-resolution high-angle annular dark field scanning transmission electron microscopy (HAADF-STEM) image processed with the average background subtraction filter[27]. The atomic columns were identified according to contrast intensities, giving the atomic number of each element. A unit cell has been superimposed as a guide. The CsPbX$_3$ single-crystal pillars had near square cross sections (Fig. 1c and Supplementary Fig. 2). The corresponding chemical composition was examined by energy-dispersive X-ray spectroscopy (Supplementary Fig. 3). Quantitative in situ compressive experiments were then conducted with a scanning electron microscope (SEM). A flat punch diamond indenter (Fig. 1d) was used to apply a load and deform the CsPbX$_3$ single crystals (Fig. 1e).

Morphing can be achieved well by the family of single-crystal CsPbX$_3$ perovskites. Figure 1f–k demonstrates various examples extracted from Supplementary Video 1. Schematic diagrams of the original and morphed geometries are shown beside each sample. Figure 1f demonstrates a 'cubic' shape (front view) achieved with a CsPbBr$_3$ single crystal. The corresponding nominal compressive strain reached ~75% (Supplementary Fig. 11). Interestingly, the crystal showed little lateral thickening since the deformation was accommodated by alternating slips on a pair of conjugate slip systems. In the deformation of the CsPbBr$_3$ single crystal shown in Fig. 1g, the slips were continuously activated on a single slip system, so that the crystal was facilely deformed into an upside-down L shape. The CsPbBr$_3$ single crystal in Fig. 1h was first morphed into a distinct Z shape and eventually became almost flat and rectangular as it was spread on the substrate (Fig. 1h inset). It was like a 'fallen domino' with an astonishing nominal compressive strain of ~83%. Figure 1i illustrates that a thick CsPbBr$_3$ single crystal with a width and thickness of 1.85 µm can also achieve multislipping. It was morphed into a 'wine glass' shape. A 'rectangular arch' geometry was achieved with a CsPbCl$_3$ single crystal (Fig. 1j). The process of morphing a CsPbI$_3$ single-crystal pillar into an L shape is shown in Fig. 1k.

The experiments showed that this morphing of CsPbX$_3$ single crystals was achieved by continuous slips with multiple slip systems (multislipping). A paradigm of deformation in CsPbX$_3$ single crystals is presented in Fig. 2. We extracted a series of SEM snapshots (Fig. 2a–h) from a video of in situ compression (Supplementary Video 2) of a CsPbBr$_3$ single-crystal pillar. It was strikingly morphed into an L shape through 'domino-like' successive slips on multiple systems, as highlighted by the coloured illustrations below each snapshot. The SEM snapshots are labelled on the engineering stress versus strain curve (Fig. 2i), which shows steep drops in the stress and strain bursts caused by continuous slips followed by 'elastic re-loading'[28]. These segments give an average yield stress of ~235 ± 23 MPa and a critical resolved shear stress of ~117 ± 12 MPa. Their slopes give an average Young's modulus of 22.9 ± 2.7 GPa, which is comparable with the theoretical value for the material[29]. The stress drops that fall nearly to zero indicate that most of the dislocations slipped out of the single crystal with a relatively small sample volume, without accumulation[28]. All the slip activities occurred for a non-closely packed $\{110\}\langle1\bar{1}0\rangle$ slip system (Supplementary Note 2). There are four specific equivalent $\{110\}\langle1\bar{1}0\rangle$ slip systems under the present loading condition (Fig. 2j). For simplicity, they are referred to as S$_1$ (blue), S$_2$ (orange), S$_3$ (red) and S$_4$ (green). The slips were activated on multiple systems in turn with the aid of pillar re-orientation. For example, when the S$_1$ slip was in operation, the lateral movement of the pillar was restricted by the indenter and substrate[4,30]. As a result, the pillar was forced to rotate (see the angle θ in Fig. 2b). The resolved shear stress on each slip system changed, so that the S$_2$ slip became geometrically preferred and was initiated as a consequence (Fig. 2c). Further details are given in Supplementary Notes 3 and 4. The yield stresses showed no obvious increase, indicating that the alternate activation of different slips prevented dislocations from

different slip systems intersecting each other, thereby eliminating strain hardening and the consequent formation of axial cracks, thus resulting in exceptional plasticity. The deformation of CsPbI$_3$ and CsPbCl$_3$ single crystals was likewise achieved via multislipping (Figs. 2k and 1j), illustrating the general exceptional ductility of the CsPbX$_3$ family. The multislipping was verified by a molecular dynamics (MD) simulation. A model of a CsPbBr$_3$ single crystal for the MD simulation and its original stress state are shown in Fig. 2l. During compression, stress concentration (Fig. 2m) and slips (Fig. 2n) occurred on multiple slip systems at compressive strains of 9.3% and 10.3%, respectively, as indicated by the arrows.

To shed light on the underlying plastic deformation mechanism of CsPbX$_3$ perovskites, atomic-resolution HAADF-STEM characterization was conducted on a deformed CsPbBr$_3$ sample, which was carefully cut with a focused ion beam (FIB), as shown in Fig. 3a. The sample was found to be dislocation starved, and most of the slip bands did not contain any residual dislocation (Supplementary Fig. 8a). A very few residual dislocations were observed for the S$_1$ and S$_2$ slip systems (indicated by the squares in Fig. 3a). In the HAADF-STEM image of the S$_1$ dislocation (Fig. 3b), the dislocation cores were recognized by a geometric phase analysis (Supplementary Note 5) and are marked by ⊥ symbols. Clearly, a full dislocation dissociated into two partial dislocations $\mathbf{b}_1$ and $\mathbf{b}_2$ with a Burgers vector of $\frac{1}{2}\mathbf{a}\langle01\bar{1}\rangle$, as depicted by the white dashed circles. However, the partial pair was not collinearly distributed along the slip direction as expected[31]. The S$_2$ dislocation had similar behaviour as S$_1$ (Fig. 3c). To explain the dislocation configuration of CsPbBr$_3$, we calculated the generalized stacking fault energy (GSFE) profiles by first-principles density functional theory calculations[32]. As shown in Fig. 3d, the $\{110\}\langle1\bar{1}0\rangle$ slip system had the lowest energy barrier of ~243 mJ m^{-2}. Notice that there is an energy minimum near the middle of the $\{110\}\langle1\bar{1}0\rangle$ profile, suggesting a full dislocation tends to dissociate into two collinear partial dislocations. Besides, $\{001\}\langle010\rangle$ had the lowest antiphase boundary energy of ~60 mJ m^{-2}, which induced the partial pairs to align along it. Therefore, we conclude that the observed dislocation configuration is the result of a collinear dissociation of a full dislocation during deformation and the migration of a partial dislocation along $\{001\}\langle010\rangle$ ($\mathbf{b}_2^0$ to $\mathbf{b}_2$) when the sample was unloaded. Further details are given in Supplementary Note 5. Similar energy-driven dissociations and adjustments to a dislocation have been reported elsewhere[33]. The smaller Burgers vector of partial dislocations would facilitate dislocation movement. As a comparison, there is no energy minimum in the GSFE profiles in rock salt (NaCl) structured ionic crystals[34]. Although they have the same active slip systems and comparable energy barriers, they are not as deformable as CsPbX$_3$ perovskites[10].

In addition to the continuous slips enabled by the low-energy barrier, another key criterion for a ductile material is that no cleavage should be generated during a slip. As depicted in the HAADF-STEM images in Fig. 3b,c and Supplementary Fig. 8, no increment in the interlayer spacing across the slip planes was observed in the deformed samples, which suggests that there was no cleavage but high crystal cohesion upon morphing. We compare the detailed energy cost of a slippage on the $\{110\}\langle1\bar{1}0\rangle$ system with density functional theory. Figure 3e plots the total energy as a function of interlayer spacing from the original equilibrium state. Here the six curves (marked by 'dis_n') correspond to different gliding fractional displacements within the range from 0 to 0.5. The lowest energy was consistently obtained at an interlayer spacing of ~0 Å. The results demonstrate the excellent inherent crystal cohesion in CsPbBr$_3$. Compared with van der Waals semiconductors, in which the interlayer separation varies widely during slipping[19], the crystal cohesion in CsPbBr$_3$ makes it less prone to cleavage. Besides, from the calculation, the slip energy E_S (energy barrier) and the cleavage energy E_C (defined by the difference between the energy barrier and the energy at an infinite interlayer distance) are determined as 0.021 and 0.098 eV per atom, respectively. The inequality $E_S \ll E_C$ suggests
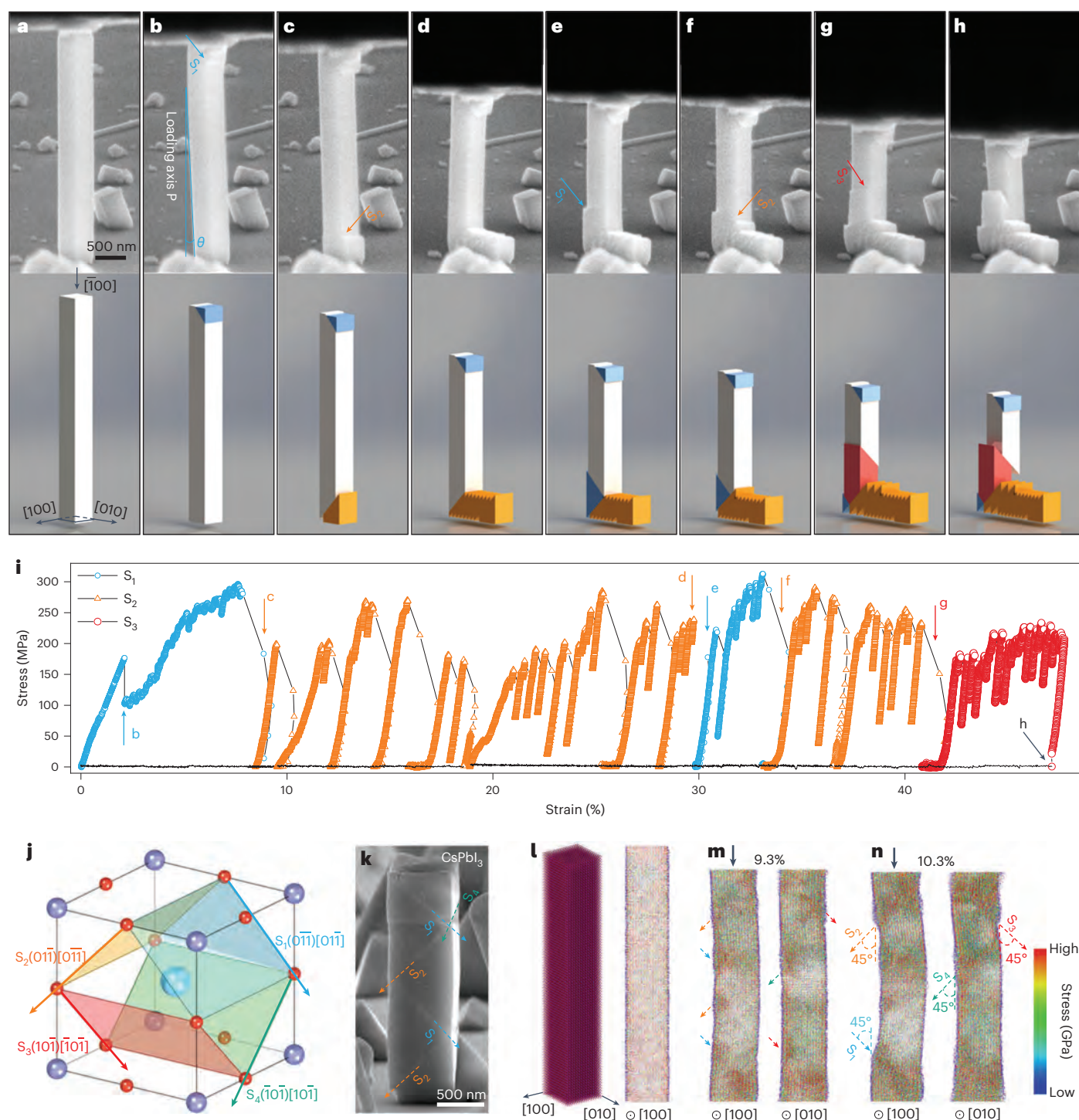
Fig. 2 | Morphing a CsPbBr₃ single crystal through successive multislips.
a–h, SEM snapshots of the in situ compression process, showing the original pillar (**a**), the activation of S_1 slip (**b**), S_2 slip (**c**), and continuous S_2 slips (**d**), another S_1 slip (**e**), S_2 slip (**f**) and S_3 slip (**g**) with final geometry (**h**). Diagrams illustrating the pillar geometries for each snapshot are given below. Different colours highlight the activation of different slip systems. **i**, Engineering stress versus strain curve coloured according to the active slip system. The snapshots

in **a–h** are labelled. **j**, A unit cell of CsPbBr₃ showing four equivalent $\{110\}\langle 1\bar{1}0\rangle$ slip systems under the current loading geometry. These are as S_1 (blue), S_2 (orange), S_3 (red) and S_4 (green). **k**, Deformed CsPbI₃ single crystal showing multislipping. **l**, Model of a CsPbBr₃ single crystal used in the MD simulation (left) and its stress state before compression (right). **m,n**, Stress states of the crystal at 9.3% (**m**) and 10.3% (**n**) compression strain, respectively, with projection views along [100] (left) and [010] (right). The multiple slips are indicated by the coloured arrows.

that our crystals can easily deform through slips while maintaining their structural integrity without cleaving.

To determine the physical origin of the observed deformability and the energy profiles, we conducted detailed electronic and structural analyses. The electron localization functions of CsPbBr₃

(Fig. 3f,g) indicate that more electrons tend to populate between Br and Pb atoms than other pairs, leading to the strong covalent bond Br–Pb, which can maintain crystal cohesion and prevent the crystal from cleaving. The electron localization functions of CsPbCl₃ and CsPbI₃ also indicate that electrons are localized between Cl–Pb and
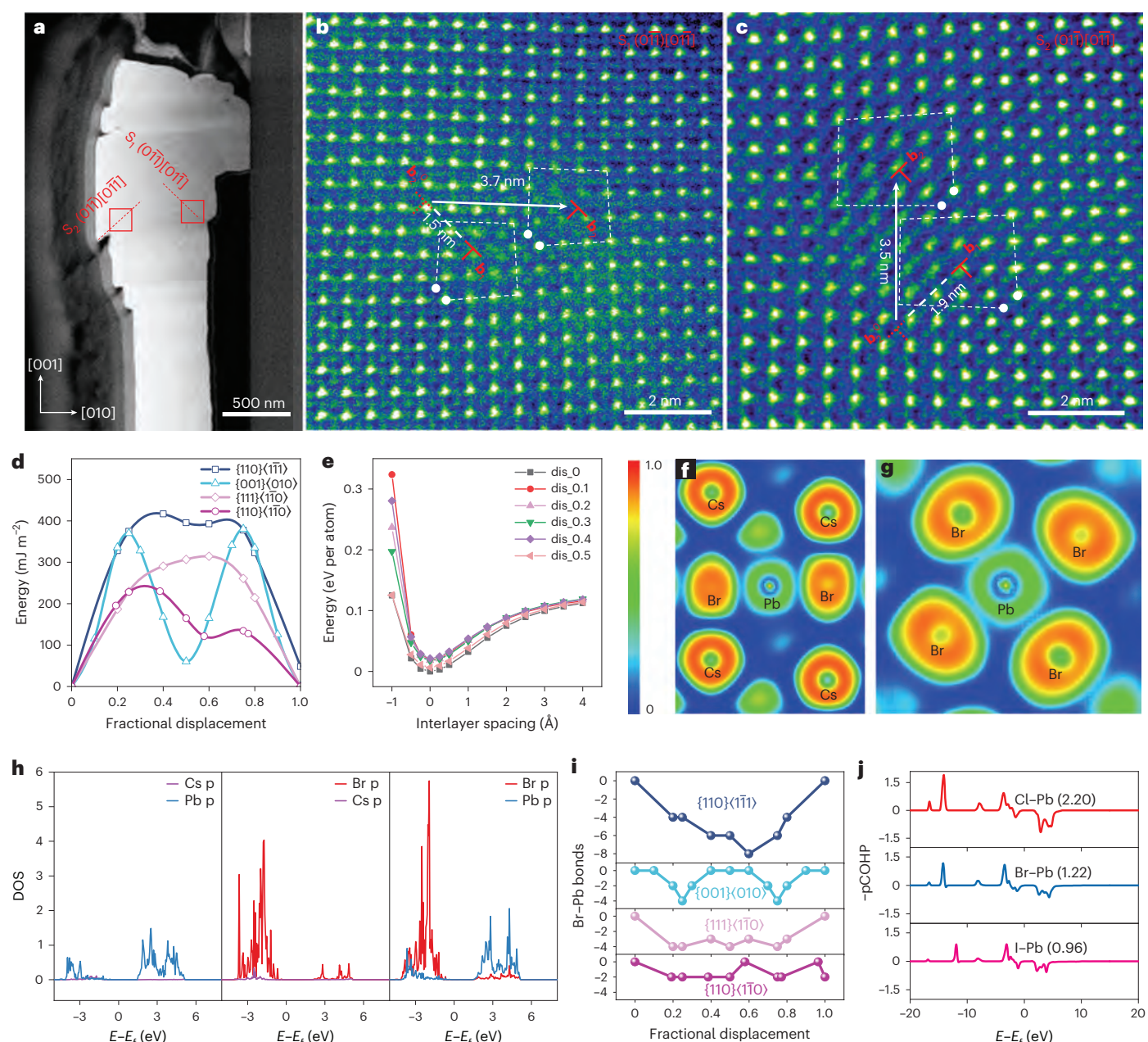
Fig. 3 | Deformation mechanism and the origin of the exceptional plasticity of CsPbX₃ perovskites. a, Thin slice sample fabricated from a deformed CsPbBr₃ single crystal. **b,c**, HAADF-STEM images taken from S₁ (**b**) and S₂ (**c**), as indicated in **a**, showing the dislocation configuration. **d**, GSFE profiles of several low-index slip systems in CsPbBr₃, suggesting that {110}⟨1̄10⟩ has the lowest energy barrier. **e**, Energy as a function of interlayer spacing relative to the original equilibrium state. Curves correspond to six different fractional displacements (ranging from

0 to 0.5), as marked by 'dis_*n*'. **f,g**, Electron localization functions for the [011]pc projection (**f**) and the [100]pc projection (**g**) in CsPbBr₃. **h**, Density of states (DOS) of bonding atoms in CsPbBr₃. **i**, Br–Pb bond numbers as a function of fractional displacement when slipping along different systems. **j**, Projected crystal orbital Hamilton populations (pCOHP) of X–Pb bonds in CsPbX₃. The integration of pCOHP from negative infinity to the Fermi level is denoted in parentheses.

I–Pb bonds (Supplementary Fig. 10). Moreover, in the density of states of bonding atoms (Fig. 3h), the peaks of Pb and Br overlap at –3.0 eV, whereas the overlaps between Cs–Pb and Br–Cs are negligible. A linear model confirms that Br–Pb bonds play a key role in deformation (Supplementary Note 6). Therefore, we evaluated the variation of Br–Pb bond numbers in the faulted region when shearing along different slip systems (Fig. 3i). The results explain the trend of energy profiles in Fig. 3d well. For example, the bond number changes least along {110}⟨1̄10⟩, leading to the lowest shear resistance. Furthermore, we compared the strength within the CsPbX₃ family by projecting their crystal orbital Hamilton populations onto X–Pb bonds and integrating

to the Fermi level (Fig. 3j). The bond strengths show a trend of Cl–Pb > Br–Pb > I–Pb, which is consistent not only with the experimentally measured yield stresses and Young's moduli of CsPbX₃ but also with the {110}⟨1̄10⟩ energy barriers, namely ~384 mJ m⁻² (CsPbCl₃), ~243 mJ m⁻² (CsPbBr₃) and ~210 mJ m⁻² (CsPbI₃); see Supplementary Note 7. These energy barriers are sufficiently low compared with other perovskite materials (for example, ~1,230 mJ m⁻² in SrTiO₃)[31], so that together with the strong X–Pb bonds, CsPbX₃ undergoes continuous slips while maintaining its crystal integration and cohesion. Exceptional plasticity can, thus, be consistently achieved in samples with a range of diameter and aspect ratios, even though the observations
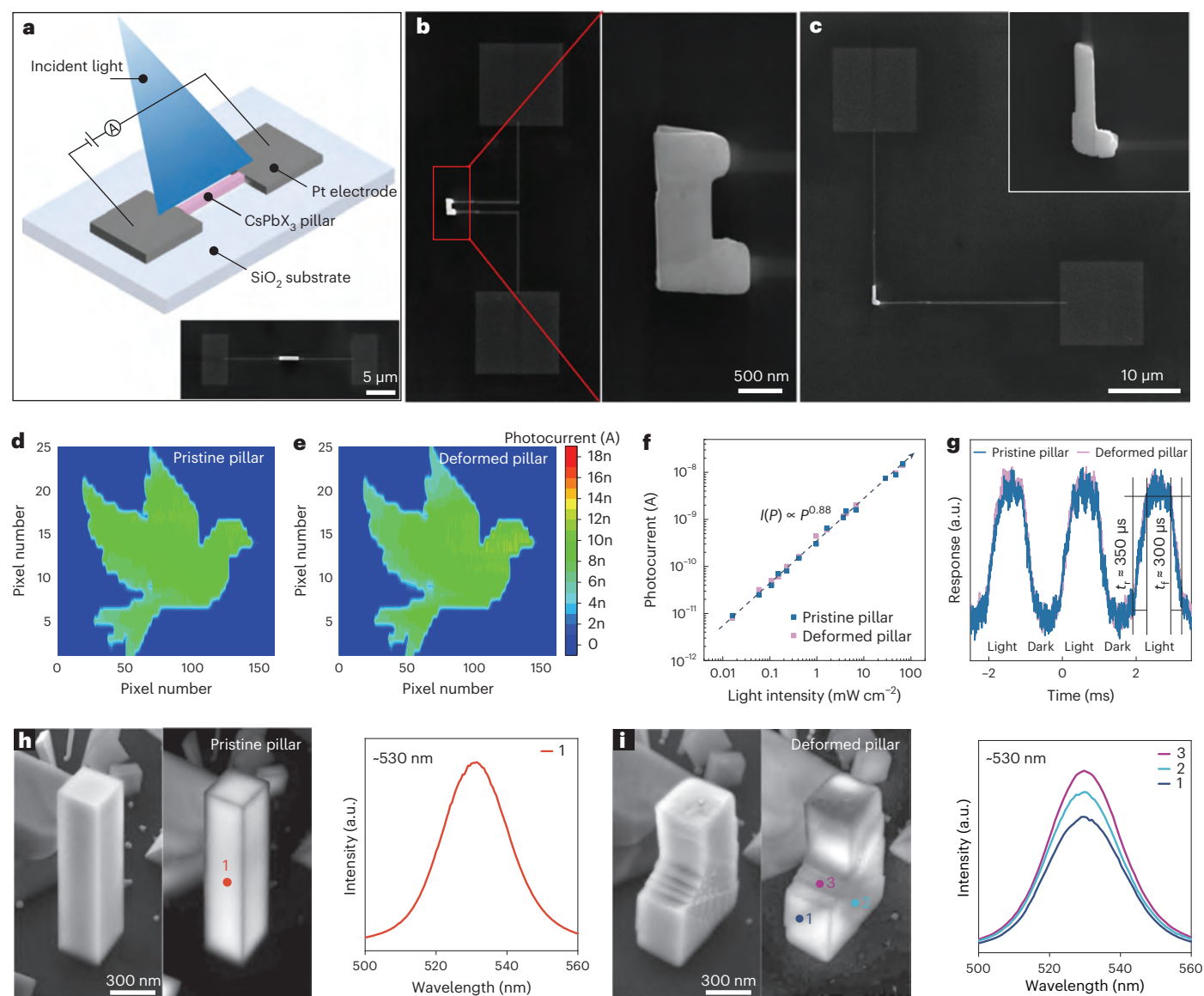
Fig. 4 | Application of the morphed CsPbX₃ crystals to construct patterned photodetector devices and optoelectronic performance characterization. a, Basic configuration of a photodetector. The inset shows a photodetector based on a pristine pillar. **b,c**, Variform photodetectors fabricated from morphed pillars with rectangular arch (**b**) and L shape (**c**) geometries. **d,e**, Two-dimensional photocurrent maps produced with a hollow mask in the shape of a 'peace dove' for a pristine pillar (**d**) and a deformed pillar (**e**), where n represents nano-. **f**, Photocurrent versus light intensity (I–P), showing a power law $I(P) \propto P^{0.88}$.

g, Transient photoresponses of pristine and deformed pillars under a chopping frequency of 500 Hz. **h**, SEM image (left) and CL image (middle) of an as-fabricated CsPbBr₃ pillar, and the corresponding CL spectrum (right) showing an intrinsic emission peak at ~530 nm. **i**, SEM image (left) and CL image (middle) of the same pillar after being compressed to 30% strain. Right, the CL spectra from three different deformed regions had almost the same emission peaks. a.u. arbitrary units.

were limited to micro-sized samples, giving an average slip-mediated strain of ~64% ± 8% (Supplementary Fig. 13).

We further demonstrated that this kind of plastic morphing can be applied in constructing patterned photodetector devices (Fig. 4a) with undegraded performance. Variform photodetectors were fabricated according to the geometries of morphed pillars (Fig. 4b,c). As expected, their photocurrent was comparable with that of the pristine pillars (Supplementary Fig. 14). We then measured the image-sensing ability of photodetectors based on pristine and deformed pillars (Methods). Their two-dimensional photocurrent maps of a 'peace dove' shaped hollowed mask exhibited almost the same pattern and intensity (Fig. 4d,e). More importantly, these two kinds of photodetectors followed the same power law relation of $I(P) \propto P^{0.88}$, where I is the photocurrent and P is the incident light intensity (Fig. 4f). The transient photoresponse

of pristine and deformed pillars was also measured under a chopping frequency of 500 Hz, both photodetectors had a rise time t_r of ~350 μs and a fall time t_f of ~300 μs (Fig. 4g). The almost same optoelectronic performance in deformed pillars indicated unchanged electron–hole generation and recombination and carrier–carrier interactions, due to the unchanged microstructure. To assess the impact of deformation on the electronic properties of CsPbX₃ single crystals, in situ cathodoluminescence (CL) characterization was conducted. Figure 4h has SEM and CL images of an as-fabricated CsPbBr₃ pillar. The corresponding CL spectrum shows a typical emission peak at ~530 nm, which refers to intrinsic bandgap energy of ~2.34 eV (ref. 35). After the pillar was compressed into an L shape by ~30% compressive strain (Fig. 4i), the local CL spectra obtained from three deformed regions consistently give a peak at ~530 nm, the value is almost the same as that before

deformation. An additional example showing a similar result is shown in Supplementary Fig. 15. The unaffected optoelectronic performance and bandgap in morphed $CsPbX_3$ single crystals may also render potential applications in deformable devices.

Our results demonstrate that all-inorganic $CsPbX_3$ perovskite single crystals can be substantially deformed and facilely morphed into distinct geometries and shapes through successive, 'domino-like' multislipping under ambient conditions, without damaging their crystalline integrity, lattice structure or attractive optoelectronic properties. In comparison with the plastic deformation mechanisms of other ductile semiconductors, our findings suggest that micro-sized ionic $CsPbX_3$ perovskites, as a class of intrinsic ductile inorganic semiconductors, have enormous application potential for manufacturing next-generation deformable electronics, optoelectronics and energy devices.

Online content

Any methods, additional references, Nature Portfolio reporting summaries, source data, extended data, supplementary information, acknowledgements, peer review information; details of author contributions and competing interests; and statements of data and code availability are available at https://doi.org/10.1038/s41563-023-01631-z.

References

1. Oh, J. Y. et al. Intrinsically stretchable and healable semiconducting polymer for organic transistors. *Nature* **539**, 411–415 (2016).
2. Root, S. E., Savagatrup, S., Printz, A. D., Rodriquez, D. & Lipomi, D. J. Mechanical properties of organic semiconductors for stretchable, highly flexible, and mechanically robust electronics. *Chem. Rev.* **117**, 6467–6499 (2017).
3. Chen, H. et al. Room-temperature plastic inorganic semiconductors for flexible and deformable electronics. *InfoMat* **3**, 22–35 (2021).
4. Hertzberg, R. W., Vinci, R. P. & Hertzberg, J. L. *Deformation and Fracture Mechanics of Engineering Materials* (John Wiley & Sons, 2020).
5. Zhang, H. et al. Approaching the ideal elastic strain limit in silicon nanowires. *Sci. Adv.* **2**, e1501382 (2016).
6. Dang, C. et al. Achieving large uniform tensile elasticity in microfabricated diamond. *Science* **371**, 76–78 (2021).
7. Wei, B. et al. Size-dependent bandgap modulation of ZnO nanowires by tensile strain. *Nano Lett.* **12**, 4595–4599 (2012).
8. Li, X. et al. High elasticity of $CsPbBr_3$ perovskite nanowires for flexible electronics. *Nano Res.* **14**, 4033–4037 (2021).
9. Chen, M. et al. Achieving micron-scale plasticity and theoretical strength in silicon. *Nat. Commun.* **11**, 2681 (2020).
10. Zou, Y. & Spolenak, R. Size-dependent plasticity in micron- and submicron-sized ionic crystals. *Philos. Mag. Lett.* **93**, 431–438 (2013).
11. Fujikane, M., Nagao, S., Chrobak, D., Yokogawa, T. & Nowak, R. Room-temperature plasticity of a nanosized GaN crystal. *Nano Lett.* **21**, 6425–6431 (2021).
12. Mathews, N. G., Saxena, A. K., Kirchlechner, C., Dehm, G. & Jaya, B. N. Effect of size and domain orientation on strength of barium titanate. *Scr. Mater.* **182**, 68–73 (2020).
13. Liu, Y. et al. Giant room temperature compression and bending in ferroelectric oxide pillars. *Nat. Commun.* **13**, 335 (2022).
14. Yang, K. H., Ho, N. J. & Lu, H. Y. Plastic deformation of ⟨001⟩ single-crystal $SrTiO_3$ by compression at room temperature. *J. Am. Ceram. Soc.* **94**, 3104–3111 (2011).
15. Stich, S. et al. Room-temperature dislocation plasticity in $SrTiO_3$ tuned by defect chemistry. *J. Am. Ceram. Soc.* **105**, 1318–1329 (2022).
16. Li, Y. et al. Theoretical insights into the Peierls plasticity in $SrTiO_3$ ceramics via dislocation remodelling. *Nat. Commun.* **13**, 6925 (2022).
17. Gumbsch, P., Taeri-Baghbadrani, S., Brunner, D., Sigle, W. & Rühle, M. Plasticity and an inverse brittle-to-ductile transition in strontium titanate. *Phys. Rev. Lett.* **87**, 085505 (2001).
18. Oshima, Y., Nakamura, A. & Matsunaga, K. Extraordinary plasticity of an inorganic semiconductor in darkness. *Science* **360**, 772–774 (2018).
19. Shi, X. et al. Room-temperature ductile inorganic semiconductor. *Nat. Mater.* **17**, 421–426 (2018).
20. Wei, T.-R. et al. Exceptional plasticity in the bulk single-crystalline van der Waals semiconductor InSe. *Science* **369**, 542–545 (2020).
21. Wang, H. et al. Orientation-dependent large plasticity of single-crystalline gallium selenide. *Cell Rep. Phys. Sci.* **3**, 100816 (2022).
22. Zhang, J., Hodes, G., Jin, Z. & Liu, S. All-inorganic $CsPbX_3$ perovskite solar cells: progress and prospects. *Angew. Chem. Int. Ed.* **58**, 15596–15618 (2019).
23. Fu, Y. et al. Metal halide perovskite nanostructures for optoelectronic applications and the study of physical properties. *Nat. Rev. Mater.* **4**, 169–188 (2019).
24. Wang, Y. et al. Thermodynamically stabilized β-$CsPbI_3$-based perovskite solar cells with efficiencies >18%. *Science* **365**, 591–595 (2019).
25. Meng, Y. et al. Direct vapor-liquid-solid synthesis of all-inorganic perovskite nanowires for high-performance electronics and optoelectronics. *ACS Nano* **13**, 6060–6070 (2019).
26. Steele, J. A. et al. Thermal unequilibrium of strained black $CsPbI_3$ thin films. *Science* **365**, 679–684 (2019).
27. Kilaas, R. Optimal and near-optimal filters in high-resolution electron microscopy. *J. Microsc.* **190**, 45–51 (1998).
28. Greer, J. R., Oliver, W. C. & Nix, W. D. Size dependence of mechanical properties of gold at the micron scale in the absence of strain gradients. *Acta Mater.* **53**, 1821–1830 (2005).
29. Roknuzzaman, M., Ostrikov, K., Wang, H., Du, A. & Tesfamichael, T. Towards lead-free perovskite photovoltaics and optoelectronics by ab-initio simulations. *Sci. Rep.* **7**, 14025 (2017).
30. Wang, Q., Wang, J., Li, J., Zhang, Z. & Mao, S. X. Consecutive crystallographic reorientations and superplasticity in body-centered cubic niobium nanowires. *Sci. Adv.* **4**, eaas8850 (2018).
31. Hirel, P., Marton, P., Mrovec, M. & Elsässer, C. Theoretical investigation of {110} generalized stacking faults and their relation to dislocation behavior in perovskite oxides. *Acta Mater.* **58**, 6072–6079 (2010).
32. Zhao, S., Stocks, G. M. & Zhang, Y. Stacking fault energies of face-centered cubic concentrated solid solution alloys. *Acta Mater.* **134**, 334–345 (2017).
33. Wu, Z. & Curtin, W. A. The origins of high hardening and low ductility in magnesium. *Nature* **526**, 62–67 (2015).
34. Nakamura, A. et al. First-principles calculations on slip system activation in the rock salt structure: electronic origin of ductility in silver chloride. *Philos. Mag.* **97**, 1281–1310 (2017).
35. Caicedo-Dávila, S. et al. Spatial phase distributions in solution-based and evaporated Cs–Pb–Br thin films. *J. Phys. Chem. C* **123**, 17666–17677 (2019).

Methods

Fabrication of CsPbX₃ (X = Cl, Br, I) single-crystal pillars

The vapour–liquid–solid synthesis method was used to fabricate $CsPbX_3$ single-crystal pillars[25]. To prepare the growth substrates, an aqueous suspension of ~150-nm-diameter Sn nanoparticles (≥99%, Aldrich) in alcohol was drop-casted onto thermally grown SiO_2/Si substrates and then naturally dried. To obtain the $CsPbX_3$ source powder, CsX (99.9%, Aldrich) and PbX_2 (99.999%, Aldrich) powders with a molar ratio of 2:1 were mixed together and then annealed (at 460 °C for $CsPbCl_3$, 430 °C for $CsPbBr_3$ and 420 °C for $CsPbI_3$) for 30 min. The $CsPbX_3$ source powder and growth substrates were placed in the high-temperature zone (470 °C for $CsPbCl_3$, 440 °C for $CsPbBr_3$ and 430 °C for $CsPbI_3$) and low-temperature zone (330 °C for $CsPbCl_3$, 300 °C for $CsPbBr_3$ and 290 °C for $CsPbI_3$), respectively, of a two-zone chemical vapour deposition system. During the growth, the chamber pressure was set to 0.8 Torr. Ar gas with a flow speed of 80 sccm was used as a carrier gas. $CsPbX_3$ pillars of various sizes then grew vertically on the growth substrates. Thin slices of deformed $CsPbBr_3$ pillars were cut with an FIB (FEI Scios Dual Beam System) for the atomic-resolution TEM analysis.

Electron microscopy characterization

Images were taken with a field-emission SEM (FEI Quanta 450 FE-SEM) operating at 10 kV. Characterization was conducted with a field-emission TEM (JEOL JEM-2100F FE-TEM) operating at 200 kV. Elemental mapping was performed with an energy-dispersive X-ray spectroscopy detector attached to the SEM and a detector attached to the TEM. Cathodoluminescence (CL) characterization was conducted with a Gatan Monarc CL detector installed on the SEM. HAADF-STEM was conducted on a spherical-aberration-corrected TEM JEOL JEM-ARM300F2. To avoid the decomposition of beam-sensitive $CsPbBr_3$ perovskites[36], a high accelerating voltage (300 kV) was used to suppress radiolysis (inelastic scattering that breaks the chemical bonds of the material)[37]. A customized electrostatic dose modulator was used to lower the electron dose rate down to 5% (~0.05 e/Å² s⁻¹) for sample protection.

In situ compression morphing

The in situ SEM compression experiments of $CsPbX_3$ pillars used a quantitative nanoindenter (Hysitron PI85 SEM PicoIndenter)[5] in conjunction with the SEM. First, a substrate on which $CsPbX_3$ pillars had been grown vertically was fixed to the stage. Then the relative position of the pillars and a flat punch diamond indenter was adjusted to ensure that they were in alignment. The in situ compression experiments were achieved by downwards movements of the diamond indenter, which was controlled by a PI85 PicoIndenter. The loading was under displacement control mode with a constant loading velocity of 20 nm s⁻¹. The load versus displacement data were read from the high-resolution indenter, whereas the displacement due to compression deformation was measured and calibrated from in situ SEM images.

Photodetector device fabrication and characterization

To fabricate photodetectors, we pushed the pristine samples and deformed samples with the nanoindenter inside the SEM so that they were lying on the SiO_2/Si substrates. We then used an FIB to coat 50-nm-thick Pt electrodes on both ends of the samples. The optoelectronic performance of the photodetectors was characterized by an Agilent 4155C semiconductor analyser with a standard probe station. The photodetectors were irradiated with a laser beam of wavelength 450 nm. The incident light power was measured by a power meter (PM400, Thorlabs). To measure the image-sensing ability of the photodetectors, a hollow mask in the shape of a 'peace dove', which was controlled by an XY planar moving stage, was placed between the incident laser and the photodetectors. The photocurrent chopped by the moving mask was recorded in real time to generate two-dimensional photocurrent maps[38]. The transient photoresponses of pristine and deformed pillars were measured by a home-built high-speed photoresponse measurement system, which had a light chopper (with a chopping frequency of 500 Hz), a current amplifier and a digital oscilloscope.

MD simulations

MD simulations were performed using the large-scale atomic/molecular massively parallel simulation (LAMMPS) code[39]. The interatomic interactions among Cs, Pb and Br were described by the short-range repulsive part of the Buckingham type and the long-range part of Coulomb interactions. The potential parameters are from previous studies[40,41]. The Ewald summation method was used to account for the long-range nature of the Coulomb forces. To simulate the compression of a crystal, we constructed supercells with a longer length along the z direction. Their cross section was square. The ratio $L_z/L_x(L_y)$ was 6. On reaching equilibrium after 150 ps at 300 K, we applied compression by deforming the simulation box. During compression, the system was relaxed using the NVT ensemble with the Nosé–Hoover thermostat at 300 K (ref. 42). The strain rate was 10^{-6} per fs.

Density functional theory calculation

The calculations were performed using the Vienna ab initio Simulation Package based on the projector-augmented-wave method[43,44]. The generalized gradient approximation in the Perdew–Burke–Ernzerhof form[45] was used to describe the exchange-correlation interactions. The energy cutoff was 350 eV. Supercells with different orientations were built to calculate the GSFE for different slip systems. The model had at least 15 atomic layers, with a 10 Å vacuum layer along the z direction. The k points were sampled with a spacing of 0.2 Å⁻¹ in all cases. The upper half of the model was continuously shifted with respect to the lower half to simulate the shear process. The stacking fault energies were calculated as the energy difference between the stacking fault structure and the perfect structure, scaled by the stacking fault area.

Data availability

The data supporting the findings of this study are available from the corresponding authors upon reasonable request.

References

36. Zhou, Y., Sternlicht, H. & Padture, N. P. Transmission electron microscopy of halide perovskite materials and devices. *Joule* **3**, 641–661 (2019).

37. Egerton, R. F., Li, P. & Malac, M. Radiation damage in the TEM and SEM. *Micron* **35**, 399–409 (2004).

38. Wang, W. et al. Mixed-dimensional anti-ambipolar phototransistors based on 1D GaAsSb/2D MoS_2 heterojunctions. *ACS Nano* **16**, 11036–11048 (2022).

39. Plimpton, S. Fast parallel algorithms for short-range molecular dynamics. *J. Comput. Phys.* **117**, 1–19 (1995).

40. Lai, M. et al. Intrinsic anion diffusivity in lead halide perovskites is facilitated by a soft lattice. *Proc. Natl Acad. Sci. USA* **115**, 11929–11934 (2018).

41. Mattoni, A., Filippetti, A. & Caddeo, C. Modeling hybrid perovskites by molecular dynamics. *J. Phys. Condens. Matter* **29**, 043001 (2016).

42. Nosé, S. A unified formulation of the constant temperature molecular dynamics methods. *J. Chem. Phys.* **81**, 511–519 (1984).

43. Blöchl, P. E. Projector augmented-wave method. *Phys. Rev. B* **50**, 17953 (1994).

44. Kresse, G. & Hafner, J. Ab initio molecular dynamics for liquid metals. *Phys. Rev. B* **47**, 558 (1993).

45. Perdew, J. P., Burke, K. & Ernzerhof, M. Generalized gradient approximation made simple. *Phys. Rev. Lett.* **77**, 3865 (1996).

Author contributions

Y.L. and X.L. conceived the research. Y.L., S.Z., F.-R.C. and J.C.H. supervised the research. X.L. performed the experiments. Y.M. synthesized the samples and investigated the optoelectronic devices. W.L. fabricated the FIB samples and performed part of the analyses. S.Z. and J.Z. performed the simulations and calculations. C.D., H.W., S.-W.H. and R.F. performed part of the analysis. X.L., Y.M., W.L., F.-R.C., S.Z., J.C.H. and Y.L. analysed the data and wrote the initial manuscript. All authors contributed to the final manuscript and approved the submission.

Competing interests

The authors declare no competing interests.

Additional information

Supplementary information The online version contains supplementary material available at https://doi.org/10.1038/s41563-023-01631-z.

Correspondence and requests for materials should be addressed to Fu-Rong Chen, Shijun Zhao, Johnny C. Ho or Yang Lu.

Peer review information *Nature Materials* thanks Karsten Durst and the other, anonymous, reviewer(s) for their contribution to the peer review of this work.

Reprints and permissions information is available at www.nature.com/reprints.